Title

Low-temperature synthesis of all-inorganic perovskite nanocrystals for UV-photodetectors

Journal

Journal of Materials Chemistry C, 7(18)

ISSN

2050-7526

Authors

Zhang, Hao

Zhang, Zihan

Ma, Chao

et al.

Publication Date

2019-05-09

DOI

10.1039/c9tc00761j

Peer reviewed

Low-Temperature Synthesis of All-Inorganic Perovskite Nanocrystals for UV-Photodetectors

Hao Zhang,[1†] Zihan Zhang, [1†] Chao Ma, [1] Yuquan Liu,[2] Haipeng Xie,[2] Shiqiang Luo,[2] Yongbo Yuan,[2] Yongli Gao,[3] Yong Zhang,[1,4] Wenquan Ming,[1,4] Yi Liu,[5] Anlian Pan,[1,6] and Bin Yang[1,7*]*

[1]College of Materials Science and Engineering, Hunan University, Changsha, Hunan 410082, China

[2]Hunan Key Laboratory of Super Microstructure and Ultrafast Process, College of Physics and Electronics, Central South University, Changsha, Hunan 410083, China

[3]Department of Physics and Astronomy, University of Rochester, Rochester, New York 14627, United States

[4]Center for High Resolution Electron Microscopy, Hunan University, Changsha, Hunan 410082, China

[5]The Molecular Foundry, Lawrence Berkeley National Laboratory, Berkeley, California 94720, United States

[6]Key Laboratory for Micro-Nano Physics and Technology of Hunan Province, Hunan University, Changsha, Hunan 410082, China

[7]Hunan Province Key Laboratory for Advanced Carbon Materials and Applied Technology, Hunan University, Changsha, Hunan 410082, China

[†]These authors contributed equally to this work

Keywords: metal halide perovskites; nanocrystals; hot-injection synthesis; photodetectors

Abstract

Controllable synthesis of tin-doped all-inorganic perovskite (e.g. $CsPbBr_3$) nanocrystals while maintaining tin at the divalent state is of great importance for not only reducing the toxicity of lead-based perovskites, but also tuning their optoelectronic properties by changing

chemical composition and geometrical size, however, it remains a nonnegligible challenge. In contradictory to the conventional high-temperature (>150 ^{o}C) synthesis reaction that would more likely facilitate oxidation of divalence Sn^{2+} to quadrivalence Sn^{4+}, this work demonstrates a facile low-temperature (105-150 ^{o}C) hot-injection method to synthesize quantum-confined Sn^{2+}-doped $CsPb_{1-x}Sn_xBr_3$ nanocrystals with tunable composition and sizes ranging from ~ 6.2 nm to ~ 8.3 nm depending on the reaction temperature. The optimized reaction temperature of 135 ^{o}C led to a Sn^{2+}-doping ratio of 3.4% in $CsPb_{1-x}Sn_xBr_3$ nanocrystals which exhibited uniform nanoplatelets with an average lateral size of ~ 7.4 nm. Furthermore, for the first time, we show that the perovskite nanocrystals are promising for the development of low-cost and trap-assisted photomultiplication UV-photodetectors, and the photodetectors based on $CsPb_{0.966}Sn_{0.034}Br_3$ nanocrystals exhibited wavelength-dependent detectivities in the magnitude of 10^{11} Jones for UV light extending from 310 nm to 400 nm at a reverse bias of -7 V. The high EQE of ~ 1940% at around 340 nm indicates that the devices had a gain at the large reverse bias condition, which is attributed to the formation of interfacial traps by $CsPb_{0.966}Sn_{0.034}Br_3$ nanocrystals that can reduce the hole injection barrier in the photodetectors for photomultiplication.

1. Introduction

Metal halide perovskites, owing to their superior properties including broadly tunable absorption,[1] exceptional defect-tolerance,[2] long carrier diffusion length,[3, 4] have been at the forefront of functional materials for low-cost and high-performance optoelectronic devices, e.g. photovoltaic cells (PVs)[5-11] and light emitting diodes (LEDs).[12-14] Compared to perovskite bulk films that have led to a certified power conversion efficiency (PCE) of 23.7% in single-junction PVs,[15] quantum-confined perovskite nanocrystals exhibit unique optical properties such as narrow width of both excitonic absorption and emission spectra along with high photoluminescence quantum yield (PLQY),[16] which are essential for LEDs and have resulted

in a high external quantum efficiency (EQE) of ~ 20% as reported very recently.[17] These high-performance LEDs are based on organic-inorganic hybrid perovskites that contain organic cations including methylammonium and formamidinium. However, due to weak hydrogen-bonding interactions between hydrogen and halogen in the organic and inorganic components, respectively,[18] these hybrid perovskites suffer from decomposition or structural changes under external attacks including heat,[19, 20] water,[21, 22] and electric fields,[23] which would negatively impact potential practical applications. All-inorganic perovskites such as cesium lead bromide ($CsPbBr_3$) nanocrystals with theoretically strong ionic bonds are expected to be more robust than organic-inorganic hybrid counterparts.[24] Partial substitution of Pb^{2+} with tin divalent ions (Sn^{2+}) is a practicable tactic for the modification of $CsPbBr_3$ nanocrystals.[26] Sn^{2+}-doping in $CsPbBr_3$ nanocrystals can tune their optoelectronic properties such as optical absorption and photoluminescence (PL).

High-temperature reaction (>150 ^oC) was often demanded in conventional synthesis of perovskite nanocrystals[27-31] to obtain nanocrystals with a variety of geometries such as nanoplatelets and nanocubes.[29] However, such high-temperature reaction facilitates oxidation of divalence Sn^{2+} to quadrivalence Sn^{4+},[32] leading to inferior optical and electrical properties of perovskite nanocrystals. It remains a great challenge to obtain $CsPb_{1-x}Sn_xBr_3$ nanocrystals with Sn at the divalent state. More importantly, tailoring chemical composition[33] and geometrical size[34] of $CsPb_{1-x}Sn_xBr_3$ nanocrystals allows efficient tuning of their electronic and optical properties including excitonic absorption spectral peaks and PL characteristics, and enables them to be potential candidates for high-performance photodetectors, which, to the best of our knowledge, is rarely reported.[35-41]

In this work, we report a facile low-temperature (105-150 ^oC) hot-injection method to synthesize $CsPb_{1-x}Sn_xBr_3$ nanoplatelets with average lateral sizes extending from ~ 6.2 nm to ~ 8.3 nm. The quantum-confined $CsPb_{1-x}Sn_xBr_3$ nanocrystals exhibit wavelength-selective excitonic absorption peaks and narrow spectral width of PL characteristics. The solution-

processed photodetectors based on the synthesized $CsPb_{0.966}Sn_{0.034}Br_3$ nanocrystals showed a detectivity in the magnitude of 10_{11} Jones for UV light ranging from 310 nm to 400 nm at a reverse bias of -7 V, which guaranteed a potential to develop sensitive UV- photodetectors.

2. Results and discussion

2.1. Synthesis and characterization of $CsPb_{1-x}Sn_xBr_3$ nanocrystals

To synthesize $CsPb_{1-x}Sn_xBr_3$ nanocrystals, a pre-heated Cs_2CO_3 precursor solution was quickly injected into a hot mixed solution of $PbBr_2$ and $SnBr_2$ with molar ratio of 2:1 at a certain temperature as oleic acid (OA) and oleylamine (OLA) were used as ligand and 1-octadecene (ODE) was the solvent. The resulted solution was cooled subsequently by an ice-water bath to obtain perovskite nanocrystals. It is worthy to note that the $PbBr_2$ and $SnBr_2$ powder mixture was completely dissolved in ODE at 105 ^oC. However, as the reaction temperature was raised to 150 ^oC, the precursor solution started to precipitate and more precipitation showed up at 170 ^oC. In order to determine whether the precipitation was related to $PbBr_2$ or $SnBr_2$ at elevated reaction temperatures, pure $PbBr_2$ and $SnBr_2$ solutions were heated separately. It was observed that the $PbBr_2$ solution remained dissolved at increasing temperature up to 190 ^oC, whereas the $SnBr_2$ solution started to precipitate at 140 ^oC. Air-sensitive trioctylphosphine (TOP) was previously used as a cosolvent to assist the dissolution of $SnBr_2$ at high temperatures.[27, 32, 42] Here, we applied a rather simple low-temperature (e.g. 105-150 ^oC) condition instead of TOP to ensure the dissolution of the $PbBr_2$ and $SnBr_2$ mixture.

For the hot-inject method, reaction temperature is generally varied to tailor geometry sizes of nanocrystals that can further govern the wavelength-selectivity of excitonic absorption and PL emissive properties. To understand the temperature-dependent tuning effect, we conducted synthesis of perovskite nanocrystals at a series of relatively low-temperatures between 105 ^oC and 150 ^oC, and both absorption and PL spectra of the obtained nanocrystal solutions were shown in **Figure 1**. It was observed that both absorption edges and excitonic absorption peaks

exhibited a typical blue-shift with decreasing reaction temperature from 150 ^{o}C to 105 ^{o}C (**Figure 1a**), which corresponded to the continuous blue-shift of PL emission peak (**Figure 1b**). The 150 ^{o}C-synthesized nanocrystals showed a moderately weak excitonic absorption peak while the corresponding PL spectrum was broad with full width at half maximum (FWHM) of ~ 35 nm and peak position at ~ 507 nm. As the reaction temperature decreased to 135 ^{o}C, an apparent excitonic absorption peak showed up at ~ 477 nm, accompanying with a narrower PL spectral peak at ~ 500 nm with smaller FWHM of ~ 24 nm. With further decreasing of the reaction temperature to 105 ^{o}C, the excitonic absorption peak moved to 470 nm, while the corresponding PL spectral peak shifted to 488 nm. It is noted that the appearance of excitonic absorption peaks with decreasing the reaction temperature is a good indication of the presence of quantum-confinement effect in perovskite nanocrystals, which agrees well with previous reports on other perovskite nanocrystals (e.g. $CsPbI_3$),[43] most likely due to the reduction in nanocrystal size with decreasing the reaction temperature. In order to examine the impact of Sn-doping on the optoelectronic properties of perovskite nanocrystals, we conducted a spectral comparison between Sn-doped and non-doped $CsPbBr_3$ nanocrystals that were synthesized under identical conditions at 135 ^{o}C. **Figure S1** shows that the Sn-doping led to a slight red-shift in the absorption spectrum, corresponding to a similar red-shift range in the PL emission peak. This observation indicates that the change of chemical composition (Sn-doping) also contributes to the variation in absorptive and emissive characteristics of $CsPbBr_3$ nanocrystals.

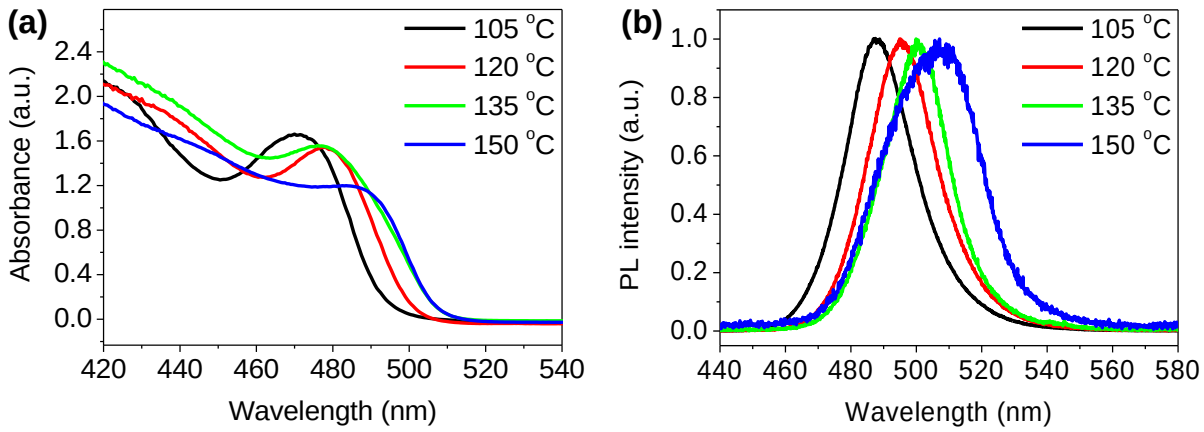

Figure 1. Absorbance (a) and photoluminescence (PL) (b) spectra of solutions of $CsPb_{1-x}Sn_xBr_3$ nanocrystals obtained at different reaction temperatures: 105 ^oC (black), 120 ^oC (red), 135 ^oC (green), and 150 ^oC (blue).

In order to confirm the existence of quantum-confined perovskite nanocrystals acquired by our low-temperature synthesis, high-resolution aberration-corrected transmission electron microscopy (TEM) was applied to examine morphology and microstructure of $CsPb_{1-x}Sn_xBr_3$ perovskite nanocrystals. As shown in the high-angle annular dark field (HAADF) scanning transmission electron microscopy (STEM) images (**Figure 2a-d)**, perovskite nanocrystals were found to exhibit variable geometry with changing the reaction temperature. As the reaction temperature was 105 ^oC, perovskite nanocrystals showed a variety of geometries including square and rectangular shapes (**Figure 2a**). The irregular perovskite nanocrystals displayed an average lateral size of ~6.2$\pm$1.9 nm, which further ensured the presence of quantum-confined effect in nanocrystals synthesized at such a low temperature. When the reaction temperature was increased to 120 ^oC, the nanocrystals still displayed an irregular geometry but the nanocrystal size showed a slight enhancement and the average crystal size reached ~ 6.8$\pm$3.9 nm (**Figure 2b**). With further increasing of the reaction temperature to 135 ^oC, the perovskite nanocrystals started to exhibit uniform square shape with an average lateral size of about ~ 7.4$\pm$2.1 nm (**Figure 2c**). We observed that higher reaction temperature of 150 ^oC resulted in non-uniformity but a slight enhancement to ~ 8.3$\pm$4.8 nm in nanocrystal size (**Figure 2d**). The HAADF-STEM images revealed that the change in nanocrystal size was a cause of the variation of both absorption and PL spectra that were observed on perovskite nanocrystal solution samples as prepared at different temperatures. Additionally, the obtained nanocrystal solutions turned from light green to dark blue by excitation of 365 nm laser (inset images of **Figure 2a-d**), which is consistent with the observation of PL spectral peaks at 488~507 nm for nanocrystals synthesized at 105-150 ^oC. The noticeable lattice fringes in individual nanocrystals as unveiled by the high-resolution bright-field TEM images (**Figure 2e**), alongside with the corresponding electron diffraction patterns (inset of **Figure 2e**), apparently demonstrated single

crystalline feature of perovskite nanocrystals. **Table S1** summarizes the synthesis temperature, doping ratio, nanocrystal size, and standard deviation for each condition. To reveal the impact of Sn-doping on the nanocrystal morphology, we acquired HAADF images from non-doped $CsPbBr_3$ nanocrystals that were synthesized under identical conditions at 135 ^oC as those of Sn-doped counterpart. As shown in **Figure S2**, the $CsPbBr_3$ nanocrystals without Sn-doping display a lightly larger size of about 7.6 ± 3.4 nm and less uniform size distribution compared to non-doped $CsPbBr_3$ nanocrystals. This observation confirms that the blue-shift of both absorption and PL spectra (**Figure S1**) is mainly caused by the Sn-doping, rather than size effect, because large nanocrystal size should lead to a red-shift in absorption and PL spectra.

The good crystallinity of perovskite nanocrystals was further confirmed with X-ray diffraction (XRD) characterization, which revealed evident X-ray reflection peaks at around $2\theta=15.2^o$, 21.5^o, 30.7^o, 37.7^o, and 43.9^o (**Figure 2f**) for $CsPbBr_3$. It is noted that the XRD pattern of the perovskite nanocrystals obtained at low reaction temperature 105 ^oC matches well with the XRD pattern of standard $CsPbBr_3$ (PDF#54-0752) whereas higher reaction temperatures (120 ^oC and 135 ^oC) resulted in a slight shift to lower 2θ angles, which could be attributed to partial substitution of Pb with Sn atoms in the $CsPbBr_3$ lattice as specifically discussed below. In cooperation with the characterization of lateral morphology by high resolution TEM, atomic force microscopy (AFM) lateral line scans were conducted to disclose the average height of nanocrystals, which was estimated to be around 2.0 nm (**Figure 2g-h**). This result suggests that the $CsPb_{1-x}Sn_xBr_3$ perovskite nanocrystals are nanoplatelets rather than nanocubes.

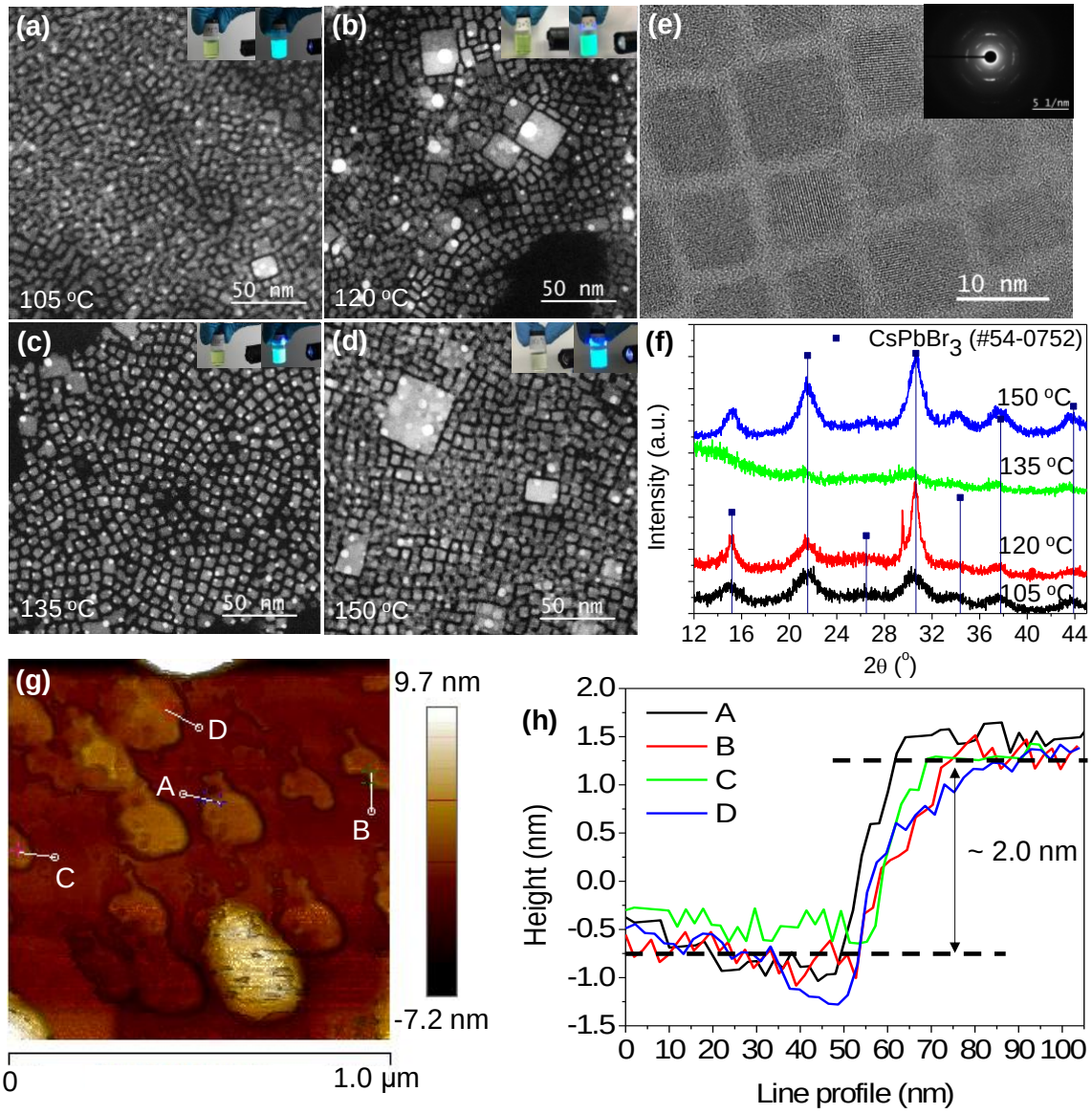

Figure 2. Morphology and microstructure of perovskite nanocrystals. Surface morphology revealed by HAADF-STEM images of nanocrystals synthesized at different temperatures: (a) 105 ^{o}C, (b) 120 ^{o}C, (c) 135 ^{o}C, (d) 150 ^{o}C. (e) High-resolution bright field TEM image and corresponding electron diffraction patterns. (f) X-ray diffraction patterns of nanocrystals synthesized at 105 ^{o}C (black), 120 ^{o}C (red), and 135 ^{o}C (green). (g) Height of perovskite nanocrystals revealed by AFM topography image and lateral line scans crossing a region that contains nanocrystals: (h) Line scan A, B, C and D are marked in the AFM topography image (g), showing the average height of nanocrystals is ~ 2.0 nm. (e) and (g) were acquired from the sample prepared at 135 ^{o}C

As mentioned above, the shift of X-ray reflection peaks may be due to partial substitution of Pb with Sn in the lattice of $CsPbBr_3$. However, it is still unclear whether and how much amount of Sn was doped into the $CsPbBr_3$ nanocrystals by XRD measurements. To prove this possible scenario and quantify the doping ratio of Sn in the $CsPb_{1-x}Sn_xBr_3$ nanocrystals, X-ray

photoelectric spectroscopy (XPS) was applied to examine the obtained perovskite nanocrystals. Additionally, since the divalent Sn^{2+} ions are possibly oxidized to quadrivalent Sn^{4+} during the synthesis process, it is important to understand whether the Sn is in divalent state in $CsPb_{1-x}Sn_xBr_3$ perovskite nanocrystals by XPS. As shown in **Figure 3a**, we observed XPS spectral peaks at 724.4 eV and 738.3 eV for Cs $3d_{5/2}$ and Cs $3d_{3/2}$, respectively, indicating the existence of Cs in perovskite nanocrystals. In addition, the respective XPS spectral peaks at 138.7 eV and 143.5 eV can be assigned to Pb $4f_{7/2}$ and Pb $4f_{5/2}$ (**Figure 3b**), signifying the presence of Pb. The presence of Br was further demonstrated by XPS spectral signals at 181.9 eV and 188.6 eV for Br $3p_{3/2}$ and Br $3p_{1/2}$, respectively (**Figure 3c**). It is important to note that the XPS spectral signals for Sn were not observed in the perovskite nanocrystals as grown at 105 ^oC, which means that little Sn was doped into perovskite nanocrystals at such a low temperature. However, with increasing the reaction temperature, we observed the presence of Sn $3d_{5/2}$ and $3d_{3/2}$ XPS peaks at 487.1 eV and 495.6 eV, respectively. These evidences suggest that Sn is not only present in perovskite nanocrystals but also in the divalent state Sn^{2+} in $CsPb_{1-x}Sn_xBr_3$, rather than quadrivalent Sn^{4+}. This observation is significant since previous studies showed that the Sn^{2+} was oxidized to Sn^{4+} when using high-temperature synthesis.[32] In our case, the Sn^{2+} was obtained without any noticeable oxidization as the reaction temperature was decreased significantly. The Sn $3d_{5/2}$ and $3d_{3/2}$ XPS signal showed up when the reaction temperature was increased to 120 ^oC (**Figure 3d**). The quantitative analysis of XPS signals between Pb and Sn reveals that as the reaction temperature was increased to 135 ^oC, the XPS spectral intensity for Sn 3d peaks was enhanced apparently, corresponding to a doping ratio of 3.4% and a formula of $CsPb_{0.966}Sn_{0.034}Br_3$. However, further increasing the reaction temperature to 150 ^oC led to the disappearance of XPS spectral signals for Sn 3d, indicating that Sn failed to be doped into the perovskite nanocrystals, most likely due to decreased solubility of $SnBr_2$ at such a high reaction temperature as discussed above. It should be pointed out that a slight shift to lower energy was observed for the XPS spectral signals of Cs, Br and Pb in the 150 ^oC synthesized sample. This

observation could be due to the change of oxidation state of Br, Pb, and Cs chemical elements in the sample; however, this possibility is unlikely since our sample was prepared under N_2 environment. Another possibility is nanocrystal size effect. HAADF images show that nanocrystal size increases with temperature, leading to the increased symmetry in the bond arrangement and thus lower pressure (or smaller binding energy) on the chemical element such as Br, Pb, and Cs in this work. Therefore, smaller energy is required to eject electrons as reflected by the shift of XPS spectral signal to lower energy. We note that for the first time our work demonstrates that the reaction temperature can not only be applied to tailor nanocrystal size, but also enables modification of composition ratio between Sn and Pb in $CsPb_{1-x}Sn_xBr_3$, both of which are critically important for tuning optoelectronic properties of perovskite nanocrystals.

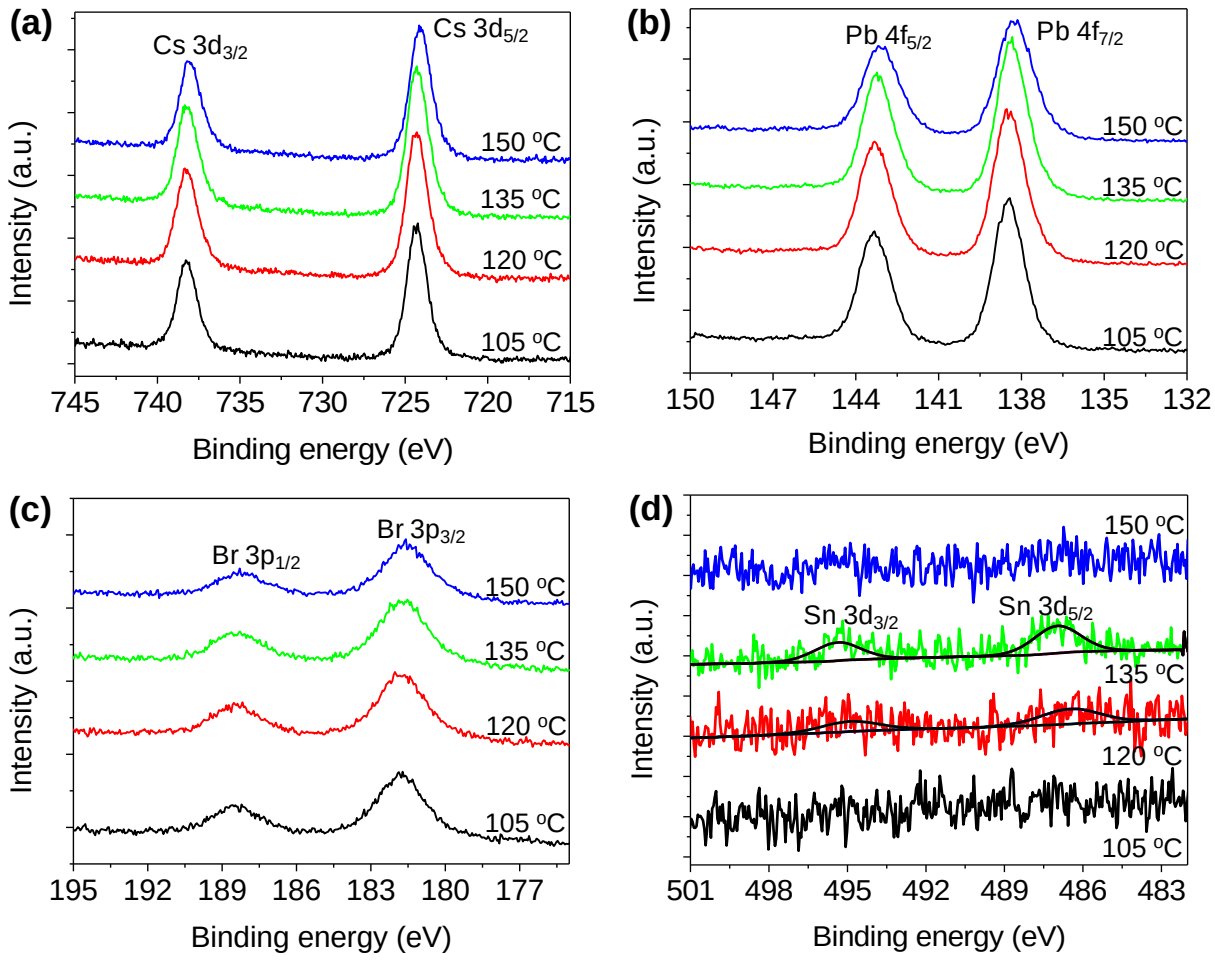

Figure 3. XPS spectra for Cs 3d (a), Pb 4f (b), Br 3p (c) and Sn 3d (d) to reveal the doping of Sn into $CsPbBr_3$ of nanocrystals synthesized at different temperatures: 105 ^oC (black), 120 ^oC

(red), 135 ^{o}C (green), and 150 ^{o}C (blue). (d) shows the apparent presence of Sn $3d_{5/2}$ and $3d_{3/2}$ XPS peaks at 487.1 eV and 495.6 eV for reaction temperatures 135 ^{o}C (green), and the fit for XPS peaks was shown with black curves.

2.2. Photodetector performance

As mentioned previously, quantum-confined perovskite nanocrystals are suitable for LEDs due to their narrow width of wavelength-selective emission spectra along with high photoluminescence quantum yield.[17] However, the composition- and size-dependent excitonic absorption spectral characteristic also makes them promising for high-performance photodetectors. In order to assess the practicability of $CsPb_{1-x}Sn_xBr_3$ nanocrystals to develop low-cost and optical-sensitive photodetectors, the optimized $CsPb_{0.966}Sn_{0.034}Br_3$ nanocrystals synthesized at 135 ^{o}C were used to fabricate photodetectors which had a device architecture of ITO/PEDOT:PSS/PVK/$CsPb_{0.966}Sn_{0.034}Br_3$: PMMA/$PC_{60}BM$/$C_{60}$/BCP/Al. A cross-section SEM image was shown in **Figure S3** to reveal the thickness of each layer in our device. In order to reduce current leaking of the photodetectors, a small amount (2 vol%) of poly(methyl methacrylate (PMMA) was blended into nanocrystals to assist the formation of continuous and compact films. **Figure S4** shows short current density-voltage (*J*-*V*) curves that were measured under both dark and illumination of 100 mW/cm^2 (AM 1.5 G). To reveal the photocurrent generation sources of the device, the incident photon-to-current efficiency (IPCE) measurements were carried out. As shown in the **Figure S5**, two peaks at 340 nm and 445 nm were observed from the bias-free external quantum efficiency (EQE) curve, which is similar with the absorption curves of C_{60} and $PC_{60}BM$ films (**Figure S6**). Thus, the photocurrent was primarily contributed by C_{60} and $PC_{60}BM$. In addition, the bias-free EQE curve displayed a shoulder peak at ~ 479 nm (**Figure S5**) which is the excitonic absorption peak position of $CsPb_{0.966}Sn_{0.034}Br_3$ nanocrystal films (**Figure S6**). Therefore, $CsPb_{0.966}Sn_{0.034}Br_3$ nanocrystals partially contributed to the photocurrent generation of the device. As shown in **Figure 4a**, with increasing the magnitude of the applied reverse bias, the EQEs at the wavelength of around 340

nm showed a monotonical enhancement and saturated at - 9 V. **Figure S7** displays the zoomed-in EQE curves which were acquired from 0 to -4 V. It was observed that the EQE values were beyond 100% as the reverse bias was increased to -5 V and the EQE was found to be ~ 1940% at a wavelength of around 340 nm and a bias of -9 V. This evidence suggests that the devices had a gain at the large reverse bias condition. In order to understand the origin of the gain, we compared the variation of EQE curves with changing bias for the devices with and without a layer of $CsPb_{0.966}Sn_{0.034}Br_3$: PMMA blend. As shown in **Figure 4b**, the maximum EQE was smaller than 60% for the device that did not have a layer of $CsPb_{0.966}Sn_{0.034}Br_3$: PMMA blend, indicating that the gain originates from $CsPb_{0.966}Sn_{0.034}Br_3$: PMMA. Furthermore, we prepared a PMMA-only layer device where the perovskite nanocrystal was not present. Interestingly, the maximum EQE was still only around 20% signifying the absence of photomultiplication effect in these devices (**Figure 4c**). Therefore, the gain originates from $CsPb_{0.966}Sn_{0.034}Br_3$ perovskite nanocrystals, rather than PMMA. In order to clarify the photomultiplication mechanism in our trap-assisted photodetector devices, **Figure 4d** illustrates the energy diagram of the device under the reverse bias and illumination condition. Previous studies have shown that such photomultiplication effect is due to the formation of interfacial traps in the devices,[44, 45] and thus it is most likely that the interfacial traps were formed at the interfaces between PVK layer and photoactive triple layers ($CsPb_{0.966}Sn_{0.034}Br_3$: PMMA/$PC_{60}BM$/$C_{60}$), where the $CsPb_{0.966}Sn_{0.034}Br_3$ nanocrystals acted as interfacial traps to reduce the electron injection barrier from the PVK layer, leading to the possible photomultiplication and gain under large electric fields. In addition, the EQE peak at 445 nm exhibited an evident red-shift with increasing the reverse bias from -6 V to -9 V, which is likely attributable to the enhanced charge collection from trap states in $PC_{60}BM$ and/or C_{60} under large electric fields.[46, 47] In order to assess whether Sn has a positive or negative influence on the photodetectors, we have prepared a reference device sample based on the Sn-free nanocrystals which were synthesized at 135 ^{o}C. **Figure S8** shows the variation of EQE curves with increasing the magnitude of reverse bias for the devices

based on Sn-free nanocrystals. It was observed that the Sn-free nanocrystals-based device also had a gain but the maximum EQE was significantly lower than that of Sn-doped counterpart, leading to lower optical detectivity. This result indicates that the Sn-doping has a positive influence to improve the device performance of photodetectors, which is most likely attributed to the easier formation of traps for Sn^{2+}-doped nanocrystals than Sn-free nanocrystals since the divalence Sn^{2+} can be oxidized to the quadrivalence Sn^{4+}.

To understand the ability of the device to measure optical signals, the wavelength-dependent photoresponsivity was obtained according to the following Equation (1).

$$R = \mathrm{EQE}\frac{\mathrm{q}\lambda}{\mathrm{hc}} \quad (1)$$

Where q is the elemental charge, λ is the optical wavelength, h is the Planck constant, and c is the speed of light in vacuum. The variation trend of photoresponsivity curves of the device is similar to that of the EQE curves, and the maximum photoresponsivity was found to be ~ 5 A/W (**Figure S9**). Based on the obtained photoresponsivity and dark current density (J_d), the specific detectivity (D^*) was estimated according to the following Equation (2).

$$D^* = \frac{\mathrm{R}}{\sqrt{2\mathrm{q}J_d}} \quad (2)$$

The maximum D^* was found in the magnitude of 10^{11} Jones for light ranging from 310 nm to 550 nm at a reverse bias of -7 V (**Figure 4e**), which is comparable or better than most of perovskite photodetectors.[35-40] The D^* showed little enhancement when the magnitude of reverse bias was larger than -7 V, most likely due to severe current leaking (large dark current) as shown in **Figure S2**. Notably, our devices were rather sensitive to UV light as suggested by D^* in the magnitude of 10^{11} Jones for UV light extending from 310 nm to 400 nm. Such feature is more obvious with increasing the magnitude of reverse bias as suggested by the merging of the apparent double peaks into nearly single peak with the peak maxima D^* of ~ 4×10^{11} Jones at 340 nm (**Figure 4e**), which is a good indication for sensitive UV-photodetectors. We characterized the variation of photocurrent as a function of irradiance intensity at an applied

bias of - 7 V. As shown in the inset of **Figure 4e**, the current varied almost linearly with irradiance intensity extending from 100 mW/cm$_2$ to 100 nW/cm$_2$, suggesting that our device can work efficiently in both high and low irradiance condition. In order to evaluate response speed of the photodetector device, we conducted transient photocurrent measurements to illustrate the rise and decay behavior with response to the illumination of 405 nm laser at a frequency of 130 Hz and an applied bias of -7 V. The response time was determined by the time interval between 10% and 90% of the maximum photocurrent of the rising portion of the photoresponse curve. As shown in **Figure 4f**, the device exhibited a response time of 1163 μs, which is similar with those of other perovskite photodetectors.[37, 41] The exponential fit for the decay curve suggested a decay time of 144 μs. The single decay channel is most likely attributed to the bimolecular recombination of photogenerated charges at the perovskite nanocrystals /PC$_{60}$BM interfaces.[48]

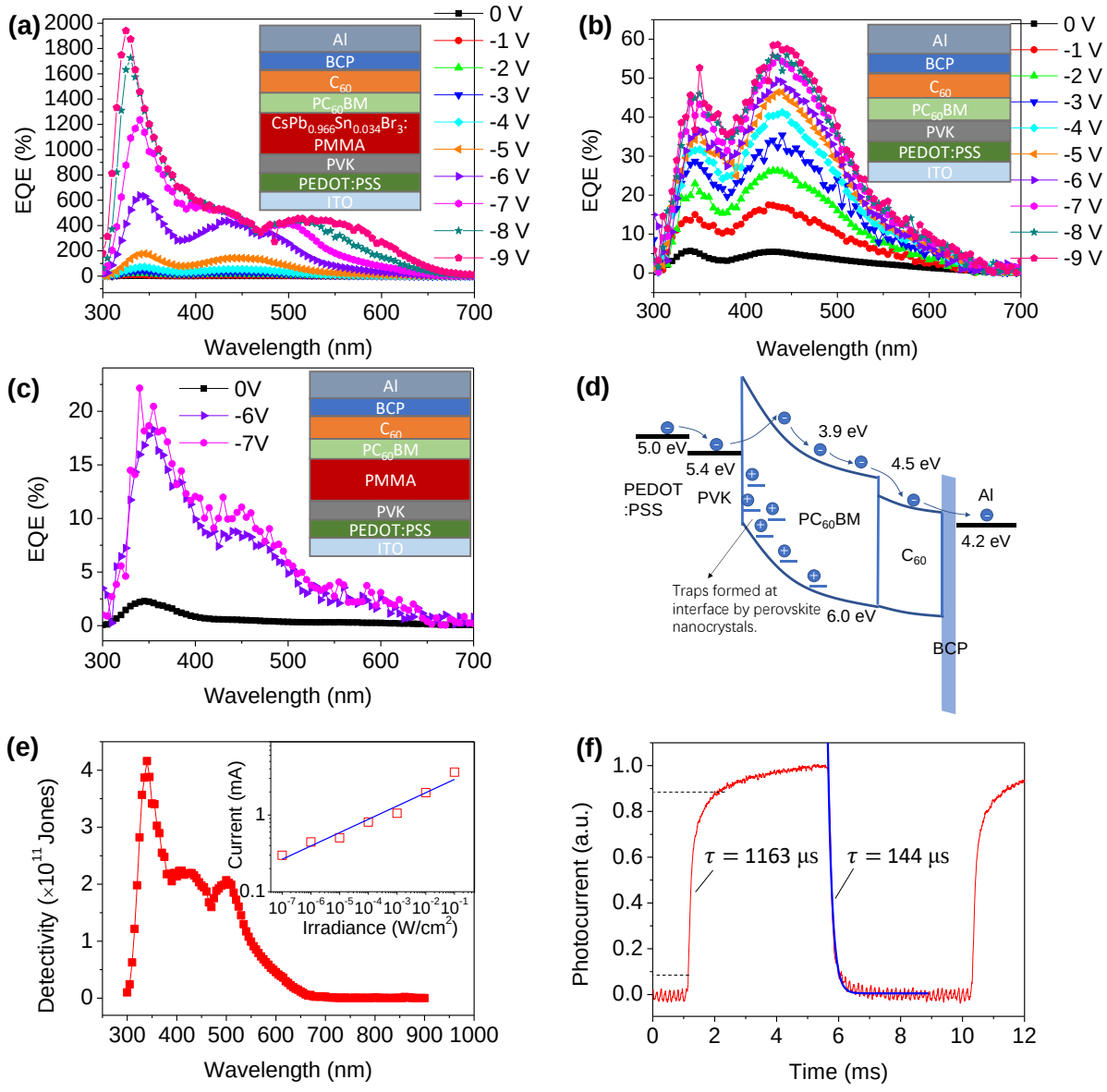

Figure 4. Device performance of photodetectors based on $CsPb_{0.966}Sn_{0.034}Br_3$ nanocrystal films. Variation of EQE curves with changing bias from 0 to -9 V for the devices that had (a) and did not have (b) a layer of $CsPb_{0.966}Sn_{0.034}Br_3$ perovskite nanocrystals: PMMA blend, and (c) PMMA-only layer, and the inset graph showing the corresponding device architecture, indicating that the gain originates from $CsPb_{0.966}Sn_{0.034}Br_3$ nanocrystals: PMMA. (d) energy diagram of the device under the reverse bias and illumination condition to show interfacial traps formed at interfaces by perovskite nanocrystals to reduce the electron injection barrier from the PVK layer. (e) Wavelength dependent detectivity and the inset figure showing the variation of current as a function of irradiance intensity measured at -7 V. (f) Transient photocurrent curve showing the rise and decay behavior of the device measured at a frequency of 130 Hz and an applied bias of -7 V, and exponential fit for the decay part (blue curve) suggesting a decay time of 144 μs. The response time was estimated to be 1163 μs by the time interval between 10% and 90% of the maximum photocurrent of the rising portion of the curve.

3. Conclusions

We have demonstrated a facile low-temperature (105-150 ^{o}C) hot-injection method to grow quantum-confined Sn^{2+}-doped $CsPb_{1-x}Sn_xBr_3$ nanocrystals that are tunable not only in geometrical sizes ranging from ~ 6.2 nm to ~ 8.3 nm but also in chemical composition (Sn^{2+}-doping ratio) by changing the reaction temperature to tune their absorptive and emissive characteristics. High-resolution STEM as combined with XPS measurements revealed that 135 ^{o}C was the optimized reaction temperature that led to uniform nanoplatelets with an average lateral size of ~ 7.4 nm and Sn^{2+}-doping ratio of ~ 3.4% in $CsPb_{1-x}Sn_xBr_3$ nanocrystals. We further showed that the composition- and size- tunable quantum-confined $CsPb_{1-x}Sn_xBr_3$ nanocrystals are promising for low-costand trap-assisted photomultiplication UV-photodetectors, which (based on $CsPb_{0.966}Sn_{0.034}Br_3$ nanocrystals) exhibited detectivities in the magnitude of 10^{11} Jones for UV light extending from 310 nm to 400 nm at a reverse bias of -7 V. As the high EQE of ~ 1940% at around 340 nm indicates a gain in the device at the large reverse bias condition, we performed a comparative study between the devices with and without a layer of $CsPb_{0.966}Sn_{0.034}Br_3$: PMMA blend, which revealed that the gain is attributable to the formation of interfacial traps by $CsPb_{0.966}Sn_{0.034}Br_3$ nanocrystals that can reduce the hole injection barrier in the photodetectors. We note that the chemical composition and geometrical size of $CsPb_{1-x}Sn_xBr_3$ nanocrystals could potentially impact device performance due to their different absorptive and emissive characteristics. In addition, both composition and size of $CsPb_{1-x}Sn_xBr_3$ nanocrystals play an important role in determining physical properties of interfacial traps and thus the magnitude of photomultiplication and gain in our devices. Further systematic studies are still needed to elucidate the role of both Sn^{2+}- doping and geometrical size of $CsPb_{1-x}Sn_xBr_3$ nanocrystals in governing the photodetection performance.

4. Experimental methods

Synthesis of perovskite nanocrystals: The Cs-oleate precursor was prepared by mixing 8 mL 1-octadecene (ODE), 0.1629 g (0.5 mmol) Cesium carbonate (Cs_2CO_3, Adamas, 99.9%) and 0.5

mL oleic acid (OA, Adamas, 90%) in a 25 mL 3-neck flask. The mixed solution was firstly heated at 120 ^{o}C for at least 30 min in N_2 environment to remove water. Subsequently, the temperature was raised to 150 ℃ and maintained for 30 min. And then, the obtained Cs-oleate precursor solution was cooled down to 120 ^{o}C in ODE in N_2 environment for the following synthesis of perovskite nanocrystals. On the other hand, 40 mL ODE, 0.368 g (1 mmol) lead(II) bromide ($PbBr_2$, Adamas, 99%) and 0.138 g (0.5 mmol) tin(II) bromide ($SnBr_2$, Alfa, 99.4%) were blended in a 100 mL 3-neck flask, and then 4 mL OA and 4 mL oleylamine (OLA, Adamas, 90%) were added. Similarly, the mixed solution was heated to 120 ^{o}C for at least 1 hour in N_2 environment to remove water. Subsequently, the temperature was raised to 105~150 °C and maintained for 30 min. As the desired reaction temperature was stabilized between 105 °C and 150 °C, the 3.2 mL as-prepared Cs-oleate precursor solution was quickly injected. After reaction for about 5 seconds, the 3-neck flask was cooled by an ice-water bath. The crude solution was centrifuged for 5 min at 3000 rpm to remove large particles. The supernatant solution and methyl acetate (MeOAc, Sinopharm, 98%) were blended with a volume ratio of 1:3. After centrifuging the mixed solution at 11000 rpm for 10 min, the precipitates were collected to wash off Cs-oleate, Pb-oleate and Sn-oleate residues with a mixed solution (3 mL, hexane: acetone=4:1 by volume ratio) and MeOAc (6 mL). Finally, the precipitate was dissolved in 5 mL hexane and centrifuged again at 4000 rpm for 5 min. The supernatant nanocrystal solution was obtained and stored in a N_2-filled glove box for further characterization and device fabrication.

Characterization of perovskite nanocrystals: The ultraviolet-visible (UV-vis) absorption spectra of perovskite nanocrystal solutions were acquired by using a Thermo scientific Evolution 201 UV-visible spectrophotometer at room temperature. The photoluminescence spectra were obtained with a Horiba iHR320 under dark environment, excited by 337 nm continuum laser. High-resolution transmission electron microscopy (TEM) images, high-angle annular dark-field (HAADF) scanning transmission electron microscopy (STEM) images, and

X-ray energy dispersive spectra (EDS) were carried out on the JEOL ARM200F microscope which was equipped with probe-forming spherical-aberration corrector. The operating voltage was 200 kV. The aperture size used in the selected area electron diffraction (SAED) is about 10 μm, corresponding to 120 nm in the image plane. The X-ray diffraction (XRD) patterns were collected using a Bruker D8 ADVANACE X-ray diffractometer with Cu-Kα radiation (λ = 1.5418 Å. The operating voltage and current was 40 kV and 40 mA, respectively. The AFM images were acquired with a Nano Scope Analysis by using the Bruker Icon atomic force microscope. The X-ray photoelectron spectroscopy (XPS) measurements were conducted on an STARPES system (SPECS) with a monochromatic SPECS XR-MF Microwave X-Ray Source (Al Kα=1486.7 eV). The cross-section SEM images were acquired on a device sample by using a Helios NanoLab G3 UC double beam electron microscope with an operating voltage of 5 kV.

Device fabrication: Clean ITO glass substrates were initially treated by UV-ozone for 10 min. The PEDOT: PSS solution (Baytron-P4083, filtered with a 0.45 μm PVDF filter) was then spin-coated onto ITO glasses at 3000 rpm for 60 seconds. The samples were subsequently baked at 135 °C for 20 min and transferred to a nitrogen-filled glovebox. Polyvinylcarbazole (PVK) solution (dissolved in 1,2-dichlorobenzene for 30 mg/mL solution) was spun cast at 4000 rpm for 20 seconds, followed by a thermal annealing treatment at 100 °C for 1 hour. The as-synthesized perovskite nanocrystal solutions were blended with a small amount (2 vol%) of polymethyl methacrylate (PMMA, dissolved in trichloromethane, 10 mg/mL). The mixed solution was spin-coated onto the PVK layer at 600 rpm for 20 seconds, followed by a thermal annealing treatment at 110 °C for 10 min. Subsequently, [6,6]-phenyl-C_{61}-butyric acid methyl ester ($PC_{60}BM$) solution (20 mg/mL in DCB) was spin-coated onto the perovskite nanocrystals: PMMA active layer at 6000 rpm for 30 seconds. The sample was then thermally-annealed at 100 °C for 1 hour. And then, 50 nm-thick C_{60} and 10 nm-thick BCP were sequentially deposited onto the sample layer-by-layer by thermal evaporation with an evaporation rate of 0.3 Å/s. The

devices were finalized by a thermal evaporation of a layer of 100 nm-thick alumina (Al) with an evaporation rate of 0.5 Å/s, and the active area was approximately 4 mm^2.

Device characterization: The photoresponse speed was measured by the transient photocurrent setup. The device was connected in series with a 10 Ω resistor which was biased at -7 V with a Keithley 2450 source meter. A 405 nm light pulse at a frequency of 130 Hz was generated by an optical chopper (Stanford Research System). An oscilloscope (LeCroy, HDO4054) was used to record the voltage variation across the resistor.

For the current-voltage (I-V) characterizations, a Newport xenon 300 W lamp was used to provide a light intensity of 100 mW/cm^2, which was calibrated with a NIST-certified Si photodiode. I-V curves were recorded by using a Keithley 2636B source meter. For the photocurrent-irradiance intensity measurements, neutral density filters were applied to adjust the light intensity from 100 mW/cm^2 to 100 nW/cm^2.

External quantum efficiencies (EQEs) were obtained with a QE-R solar cell quantum efficiency measurement system (Enli Technology). The EQE was measured at a frequency of 210 Hz. The light intensity was calibrated with a reference NIST-certified Si photodetector. The bias-dependent EQE measurements were conducted by applying reverse bias from 0 to -9 V on the devices directly.

Conflicts of interest

There are no conflicts to declare

Acknowledgements

B. Y. conceived the project and wrote the manuscript. B. Y., H. Z., Z. Z., A. P., and Y. L. designed the experiment. H. Z. synthesized nanocrystals. Z. Z. and H. Z. fabricated and

characterized the devices. C. M., Y. Z., and W. M. conducted TEM characterization. H. X., Y. L., and Y. G. performed XPS measurement. S. L. and Y. Y. measured EQE. All authors analyzed the data and reviewed the manuscript. B. Y. thanks the financial support from National Youth 1000 Talents Program, 100 Talents Program of Hunan Province, the Science and Technology Department of Hunan Province, and the research fund for the central universities. A. P. is grateful to the National Natural Science Foundation of China (Nos. 51525202 and 61574054). Y. L. was supported by the Molecular Foundry, supported by the Office of Science, Office of Basic Energy Sciences, of the U.S. Department of Energy under Contract No. DE-AC02-05CH11231. W. M. acknowledges the financial support from the National Natural Science Foundation of China (Nos. 11427806 and 51471067). The authors would like to thank Prof. Jianghua Chen for TEM and Prof. Song Liu for AFM characterizations.

References

1. M. C. Weidman, M. Seitz, S. D. Stranks and W. A. Tisdale, *ACS Nano*, 2016, **10**, 7830.
2. W. J. Yin, T. Shi and Y. Yan, *Appl. Phys. Lett.*, 2014, **104**, 6050-1429.
3. S. D. Stranks, G. E. Eperon, G. Grancini, C. Menelaou, M. J. Alcocer, T. Leijtens, L. M. Herz, A. Petrozza and H. J. Snaith, *Science*, 2013, **342**, 341-344.
4. Q. Dong, Y. Fang, Y. Shao, P. Mulligan, J. Qiu, L. Cao and J. Huang, *Science*, 2015, **347** 967-970.
5. H. Tsai, R. Asadpour, J. C. Blancon, C. C. Stoumpos, O. Durand, J. W. Strzalka, B. Chen, R. Verduzco, P. M. Ajayan, S. Tretiak, J. Even, M. A. Alam, M. G. Kanatzidis, W. Nie and A. D. Mohite, *Science*, 2018, **360**, 67.
6. H. Tan, A. Jain, O. Voznyy, X. Lan, G. D. A. Fp, J. Z. Fan, R. Quintero-Bermudez, M. Yuan, B. Zhang, Y. Zhao, F. Fan, P. Li, L. N. Quan, Y. Zhao, Z. H. Lu, Z. Yang, S. Hoogland and E. H. Sargent, *Science*, 2017, **355**, 722-726.
7. J. H. Im, I. H. Jang, N. Pellet, M. Grã¤Tzel and N. G. Park, *Nature Nanotech.*, 2014, **9**, 927-932.
8. N. J. Jeon, J. H. Noh, Y. C. Kim, W. S. Yang, S. Ryu and S. I. Seok, *Nature Mater,*, 2014, **13**, 897-903.
9. M. A. Green, A. Ho-Baillie and H. J. Snaith, *Nature Photon.*, 2014, **8**, 506-514.
10. Y. Shao, Y. Yuan and J. Huang, *Nature Energy*, 2016, **1**, 15001.
11. J. You, L. Meng, T. B. Song, T. F. Guo, Y. Yang, W. H. Chang, Z. Hong, H. Chen, H. Zhou, Q. Chen, Y. Liu, N. D. Marco and Y. Yang, *Nature Nanotech.*, 2015, **11**, 75-81.
12. Z. K. Tan, R. S. Moghaddam, M. L. Lai, P. Docampo, R. Higler, F. Deschler, M. Price, A. Sadhanala, L. M. Pazos, D. Credgington, F. Hanusch, T. Bein, H. J. Snaith and R. H. Friend, *Nature Nanotech.*, 2014, **9**, 687.
13. Q. Wang, C.-M. Wang, J.-F. Wang and S. Zhang, *Ceram. Int.*, 2016, **42**, 6993-7000.
14. Z. Xiao, R. A. Kerner, L. Zhao, N. L. Tran, K. M. Lee, T. W. Koh, G. D. Scholes and B.

P. Rand, *Nature Photon.*, 2017, **11**, 108-115.
15. https://www.nrel.gov/pv/assets/pdfs/pv-efficiency-chart.20181221.pdf.
16. M. V. Kovalenko, L. Protesescu and M. I. Bodnarchuk, *Science*, 2017, **358**, 745-750.
17. Y. Cao, N. Wang, H. Tian, J. Guo, Y. Wei, H. Chen, Y. Miao, W. Zou, K. Pan, Y. He, H. Cao, Y. Ke, M. Xu, Y. Wang, M. Yang, K. Du, Z. Fu, D. Kong, D. Dai and W. Huang, *Nature*, 2018, **562**, 249-254.
18. B. Yang, W. Ming, M.-H. Du, J. K. Keum, A. A. Puretzky, C. M. Rouleau, J. Huang, D. B. Geohegan, X. Wang and K. Xiao, *Adv. Mater.*, 2018, **30**, 1705801.
19. B. Yang, O. Dyck, W. Ming, M.-H. Du, S. Das, C. M. Rouleau, G. Duscher, D. B. Geohegan and K. Xiao, *ACS Appl. Mater. Interfaces*, 2016, **8**, 32333-32340.
20. T. W. Kim, N. Shibayama, L. Cojocaru, S. Uchida, T. Kondo and H. Segawa, *Adv. Funct. Mater.*, 2018, **28**, 1804039.
21. J. S. Yun, J. Kim, T. Young, R. J. Patterson, D. Kim, J. Seidel, S. Lim, M. A. Green, S. Huang and A. Ho-Baillie, *Adv. Funct. Mater.*, 2018, **28**, 1705363.
22. Y.-H. Kye, C.-J. Yu, U.-G. Jong, Y. Chen and A. Walsh, *J. Phys. Chem. Lett.*, 2018, **9**, 2196-2201.
23. S. Bae, S. Kim, S.-W. Lee, K. J. Cho, S. Park, S. Lee, Y. Kang, H.-S. Lee and D. Kim, *J. Phys. Chem. Lett.*, 2016, **7**, 3091-3096.
24. Y. Rakita, N. Kedem, S. Gupta, A. Sadhanala, V. Kalchenko, M. L. Böhm, M. Kulbak, R. H. Friend, D. Cahen and G. Hodes, *Cryst. Growth Des.*, 2016, **16**, 5717-5725.
25. A. Babayigit, A. Ethirajan, M. Muller and B. Conings, *Nat. Mater.*, 2016, **15**, 247.
26. Z. Du, D. Fu, T. Yang, Z. Fang, W. Liu, F. Gao, L. Wang, Z. Yang, J. Teng, H. Zhang and W. Yang, *J. Mater. Chem. C*, 2018, **6**, 6287-6296.
27. H.-C. Wang, S.-Y. Lin, A.-C. Tang, B. P. Singh, H.-C. Tong, C.-Y. Chen, Y.-C. Lee, T.-L. Tsai and R.-S. Liu, *Angew Chem. Int. Ed.*, 2016, **55**, 7924-7929.
28. L. Protesescu, S. Yakunin, M. I. Bodnarchuk, F. Krieg, R. Caputo, C. H. Hendon, R. X. Yang, A. Walsh and M. V. Kovalenko, *Nano Lett.*, 2015, **15**, 3692-3696.
29. A. Pan, B. He, X. Fan, Z. Liu, J. J. Urban, A. P. Alivisatos, L. He and Y. Liu, *ACS Nano*, 2016, **10**, 7943-7954.
30. Y. Wang, M. Zhi, Y.-Q. Chang, J.-P. Zhang and Y. Chan, *Nano Lett.*, 2018, **18**, 4976-4984.
31. M. J. Jurow, T. Lampe, E. Penzo, J. Kang, M. A. Koc, T. Zechel, Z. Nett, M. Brady, L.-W. Wang, A. P. Alivisatos, S. Cabrini, W. Brütting and Y. Liu, *Nano Lett.*, 2017, **17**, 4534-4540.
32. H.-C. Wang, W. Wang, A.-C. Tang, H.-Y. Tsai, Z. Bao, T. Ihara, N. Yarita, H. Tahara, Y. Kanemitsu, S. Chen and R.-S. Liu, *Angew.Chem. Int. Ed.*, 2017, **56**, 13650-13654.
33. X. Zhang, W. Cao, W. Wang, B. Xu, S. Liu, H. Dai, S. Chen, K. Wang and X. W. Sun, *Nano Energy*, 2016, **30**, 511-516.
34. M. C. Brennan, J. E. Herr, T. S. Nguyen-Beck, J. Zinna, S. Draguta, S. Rouvimov, J. Parkhill and M. Kuno, *J. Am. Chem. Soc.*, 2017, **139**, 12201-12208.
35. H. Deng, X. Yang, D. Dong, B. Li, D. Yang, S. Yuan, K. Qiao, Y.-B. Cheng, J. Tang and H. Song, *Nano Lett.*, 2015, **15**, 7963-7969.
36. Y. Dong, Y. Gu, Y. Zou, J. Song, L. Xu, J. Li, J. Xue, X. Li and H. Zeng, *Small*, 2016, **12**, 5622-5632.
37. C. Ma, Y. Shi, W. Hu, M.-H. Chiu, Z. Liu, A. Bera, F. Li, H. Wang, L.-J. Li and T. Wu, *Adv. Mater.*, 2016, **28**, 3683-3689.
38. M. I. Saidaminov, M. A. Haque, J. Almutlaq, S. Sarmah, X.-H. Miao, R. Begum, A. A. Zhumekenov, I. Dursun, N. Cho, B. Murali, O. F. Mohammed, T. Wu and O. M. Bakr, *Adv. Opt. Mater.*, 2017, **5**, 1600704.
39. G. Tong, H. Li, D. Li, Z. Zhu, E. Xu, G. Li, L. Yu, J. Xu and Y. Jiang, *Small*, 2018, **14**, 1702523.

40. A. Waleed, M. M. Tavakoli, L. Gu, S. Hussain, D. Zhang, S. Poddar, Z. Wang, R. Zhang and Z. Fan, *Nano Lett.*, 2017, **17**, 4951-4957.
41. C. Xie and F. Yan, *J. Mater. Chem. C*, 2018, **6**, 1338-1342.
42. G. Nedelcu, L. Protesescu, S. Yakunin, M. I. Bodnarchuk, M. J. Grotevent and M. V. Kovalenko, *Nano Lett.*, 2015, **15**, 5635-5640.
43. A. Swarnkar, A. R. Marshall, E. M. Sanehira, B. D. Chernomordik, D. T. Moore, J. A. Christians, T. Chakrabarti and J. M. Luther, *Science*, 2016, **354**, 92-95.
44. J. Huang and Y. Yang, *Appl. Phys. Lett.*, 2007, **91**, 203505.
45. F. Guo, B. Yang, Y. Yuan, Z. Xiao, Q. Dong, Y. Bi and J. Huang, *Nat. Nanotech.*, 2012, **7**, 798.
46. B. Yang, F. Guo, Y. Yuan, Z. Xiao, Y. Lu, Q. Dong and J. Huang, *Adv. Mater.*, 2013, **25**, 572-577.
47. L. Burtone, D. Ray, K. Leo and M. Riede, *J. Appl. Phys.*, 2012, **111**, 064503.
48. D. W. de Quilettes, S. M. Vorpahl, S. D. Stranks, H. Nagaoka, G. E. Eperon, M. E. Ziffer, H. J. Snaith and D. S. Ginger, *Science*, 2015, **348**, 683-686.